Review

Reproducibility in the fabrication and physics of moiré materials

https://doi.org/10.1038/s41586-021-04173-z

Received: 16 March 2021

Accepted: 21 October 2021

Published online: 2 February 2022

Check for updates

Chun Ning Lau[1]✉, Marc W. Bockrath[1], Kin Fai Mak[2] & Fan Zhang[3]

Overlaying two atomic layers with a slight lattice mismatch or at a small rotation angle creates a moiré superlattice, which has properties that are markedly modified from (and at times entirely absent in) the 'parent' materials. Such moiré materials have progressed the study and engineering of strongly correlated phenomena and topological systems in reduced dimensions. The fundamental understanding of the electronic phases, such as superconductivity, requires a precise control of the challenging fabrication process, involving the rotational alignment of two atomically thin layers with an angular precision below 0.1 degrees. Here we review the essential properties of moiré materials and discuss their fabrication and physics from a reproducibility perspective.

Arguably the most exciting development in condensed-matter physics and materials sciences over the past few years is the rise of two-dimensional (2D) moiré materials. By taking advantage of the formation of a moiré superlattice arising from a small lattice mismatch or twist angle between two adjacent atomic layers, one can tailor the electronic, thermal, mechanical, optical and optoelectronic properties of 2D vertical heterostructures. The discovery of superconductivity and correlated insulating states in 'magic angle' twisted bilayer graphene (t-BLG)[1,2] in 2018 led to a 'gold rush' of the exploration of 2D moiré materials, which soon expanded to include, for example, twisted double bilayer graphene[3–7], monolayer graphene on bilayer graphene[8–10], transition-metal dichalcogenide (TMD) homobilayers[11–13] and heterobilayers[14–17], and rhombohedral-stacked trilayer graphene (r-TLG) aligned with hexagonal boron nitride (hBN)[18–20]. Unconventional electronic phases such as superconductivity, nematicity and magnetism have all been observed experimentally, with discoveries announced almost every week.

Alluringly, 2D moiré materials are promising for unravelling strong electronic interactions while sidestepping some of the challenges associated with traditional systems, such as heavy fermion compounds or cuprates. For instance, 2D moiré materials are chemically simple, consisting of one or two covalently bonded elements, in contrast to cuprates, which are quaternary or quinary compounds with more complex structures and phases. Moreover, one of the biggest promises of moiré materials is their in situ tunability—unlike bulk crystals whose charge densities are constants, 2D moiré materials enable, through electrostatic gating, continuous tuning of the charge density over a large range, the polarity of charge carriers (electrons versus holes) and the electronic bandwidth. Thus, one can in principle map the phase diagrams of moiré systems using only a few devices, without the complications and reproducibility issues associated with crystal synthesis.

However, the fabrication of 2D moiré devices faces its own challenges, such as the new class of disorder of inhomogeneous angles and strains across the sample. Instead of chemical complexity and reproducibility of crystal doping and synthesis, researchers are wrestling with the reproducibility and uniformity of twist angles and strains. Other factors impacting device behaviour include domain formation, the roles of the hBN substrate, lattice relaxation and reconstruction, and so on. At present, a superb device is more like an 'art piece' rather than what can be easily reproduced, thus complicating data interpretation (Fig. 1). This is, of course, not ideal—to fully realize the promise of moiré materials, device fabrication processes should be optimized, well controlled and well reproduced. In this Review, we review briefly the progress and latest developments in the field, and examine the various issues related to reproducibility, as well as the ensuing debate on the peculiar phases and their underlying mechanisms in the representative moiré systems.

Classification of moiré systems in 2D materials

A moiré pattern arises from the interference of two overlaid periodic structures, which produces a superlattice with a period that can be much larger than that of either of the original structures. The spatial period or wavelength a_m of the superlattice depends on the lattice mismatch δ and relative rotation θ between the constituent lattices. In the limit of small θ and δ, a_m is given by $a_m = a/\sqrt{\delta^2 + \theta^2}$ (Box 1), where a is the average lattice constant.

A moiré superlattice can be generated by modulating either θ or δ. Twisting, that is, overlaying two lattices at a small relative angle, is often performed on lattices of the same material (panel d in Box 1). Examples of these so-called homobilayers include the well-known t-BLG, as well as twisted double bilayer graphene, twisted TMDs, monolayer on bilayer graphene, and twisted triple layers of graphene (that is, three layers of graphene at angles of approximately 0°/1.56°/0°)[21,22]. In principle, the unit cell of such a moiré superlattice can be made arbitrarily large. In realistic devices, however, the a_m of a homobilayer is limited by the precision of the rotation stage during fabrication, as well as lattice relaxation and atomic reconstruction at small twist angles (see 'Fabrication and experimental challenges').

Alternatively, moiré superlattices can be created by overlaying two lattices with different lattice constants, which are often two different materials with a small lattice mismatch, forming so-called

[1]Department of Physics, The Ohio State University, Columbus, OH, USA. [2]Department of Physics, and School of Applied and Engineering Physics, Cornell University, Ithaca, NY, USA. [3]Department of Physics, University of Texas at Dallas, Dallas, TX, USA. ✉e-mail: lau.232@osu.edu

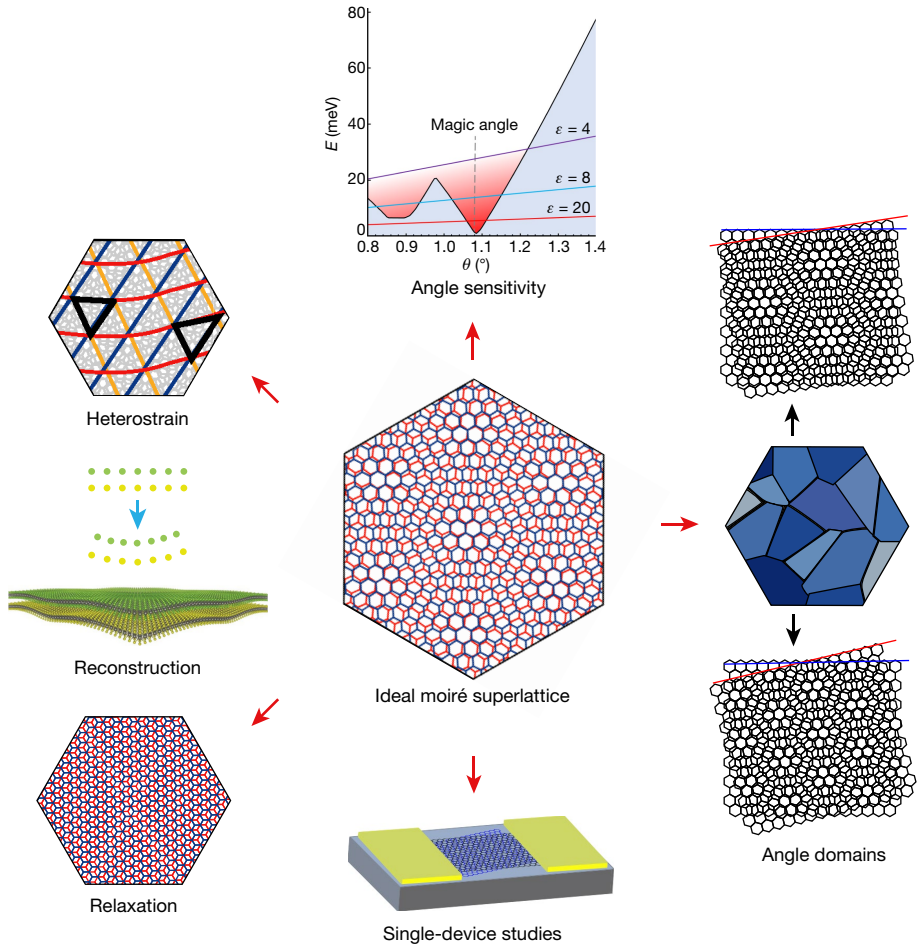

Fig. 1 | Various factors and phenomena affecting the reproducibility of moiré materials studies. Clockwise from the top, these include the following. (1) The sensitivity of homobilayers to the twist angle—samples must typically be aligned to within about 0.1° to achieve strongly correlated behaviour. The panel shows the Coulomb on-site energy (U, coloured lines shown for different dielectric constants ε) and the bandwidth (W, black lines) for t-BLG. The ratio U/W becomes >1, that is, when correlation dominates, in only a narrow range of angles around the magic value. (2) The formation of angular domains. The darker colours indicate domains with larger angles. (3) Some studies are based on data obtained from single devices. (4) Lattice relaxation can occur on heating to the ground state, for example, as shown where t-BLG reverts to Bernal stacking. (5) Atomic reconstruction can produce out-of-plane distortions of the lattice. Adapted with permission from ref. [61], Springer Nature Ltd. (6) Differential interlayer strain can both distort the moiré lattice lines as shown by the red (strongly distorted), and yellow and blue (undistorted) lines, as well as the geometry of the unit cell shown by the two black triangles (left, undistorted case; right, distorted).

heterobilayers (panel e in Box 1). Well-known examples include monolayer graphene aligned with hBN, in which the 1.8% lattice mismatch between the two materials gives rise to the Hofstadter fractal spectrum[23–28], r-TLG aligned with hBN[18–20] and TMD heterobilayers such as tungsten diselenide (WSe_2)/tungsten disulfide (WS_2)[15–17]. The $\delta = 1.8\%$ lattice mismatch between graphene and hBN limits the largest a_m to about 14 nm, whereas TMD heterobilayers have a substantially larger lattice mismatch that varies between 4% (for example, WSe_2/WS_2) and 11.7% (for example, molybdenum ditelluride ($MoTe_2$)/WS_2). For 2D materials, the formation of long-period superlattices gives rise to rich moiré band structures that can be ultraflat and topological (Box 1), and therefore electronic, optical and mechanical properties that are markedly different from their constituent materials.

Fabrication and experimental challenges

Homobilayers

For homobilayers, precision control of θ is imperative, particularly for t-BLG where correlated physics is found within only a narrow 'magic range' of approximately 0.9° to 1.2°. To overcome the challenge of assessing the precise crystal orientation of exfoliated sheets, researchers typically start from a single exfoliated atomic layer, which eliminates the need to know the absolute crystal orientation. The most successful and widely adopted technique is so-called tear and stack (Fig. 2a)[29–33]. Although simple in principle, the achieved twist angle is often not the same as that targeted with the rotation stage, owing to issues such as uneven stress and strain on the polymer and the atomic flake, undesirable flow of the polymer, precision and backlash of the stage, and lattice relaxation and 'snap-in' on assembly[34]. To reduce the strain generated during tearing, a graphene flake can be pre-cut into two or more pieces by a laser[33] or the tip of an atomic force microscope (AFM)[18,32,35,36]. The device mobility can be increased by repeated annealing of the stacks, by frequent examination via AFM or scanning electron microscope (SEM), or by using the AFM tip as a 'squeegee' to sweep impurities trapped between layers into bubbles[37].

Heterobilayers

To fabricate TMD heterobilayer moiré superlattices, one technique is to simply angle-align the sharp edges of the two different materials[25], taking advantage of the crystals' tendency to break along crystallographic directions and the spontaneous 'snap-in' of two overlaid crystals if the initial angle is small[38]. Another technique is to pre-determine

Box 1

Introduction to moiré flat bands

Graphene (r-TLG) is a Dirac semimetal with linear (cubic) band crossing (touching) and opposite winding numbers ±1 (±3) at the K/K′ valleys protected by inversion and time-reversal symmetries (panels **a**, **b**). When energy gaps are created at the K/K′ points, non-trivial Berry curvature spreads from there, giving rise to orbital magnetic moments and valley-projected band topology. Monolayer TMD can be viewed as gapped graphene with strong spin–orbit couplings and valley Chern numbers of ±1 per spin (panel **c**). With moiré engineering, such band topology[107] is regularized by superlattice gaps and turns into miniband topology[11,83–86,127]; however, this topology is still fragile to edge intervalley couplings. In momentum space, the moiré and principal reciprocal lattice vectors, $\mathbf{G}_m$ and $\mathbf{G}$, respectively, are elegantly related by $\mathbf{G}_m = \delta\mathbf{G} - \theta\hat{\mathbf{z}} \times \mathbf{G}$, where $\hat{z}$ is the out-of-plane unit vector, and thus in real space the moiré period is $a_m = a/\sqrt{\delta^2 + \theta^2}$. This implies that for a homobilayer (heterobilayer), the moiré pattern is almost rotated by 90° (barely rotated) with respect to the atomic lattices (panels **d**, **e**). The miniband structure of a homobilayer is highly sensitive to the twist angle θ (refs. [2,11]), and the correlated states can be easily destabilized by angle disorder. In contrast, the miniband structure of a heterobilayer is largely determined by the lattice mismatch δ (refs. [15,16]), and the correlated states are less sensitive to angle disorder.

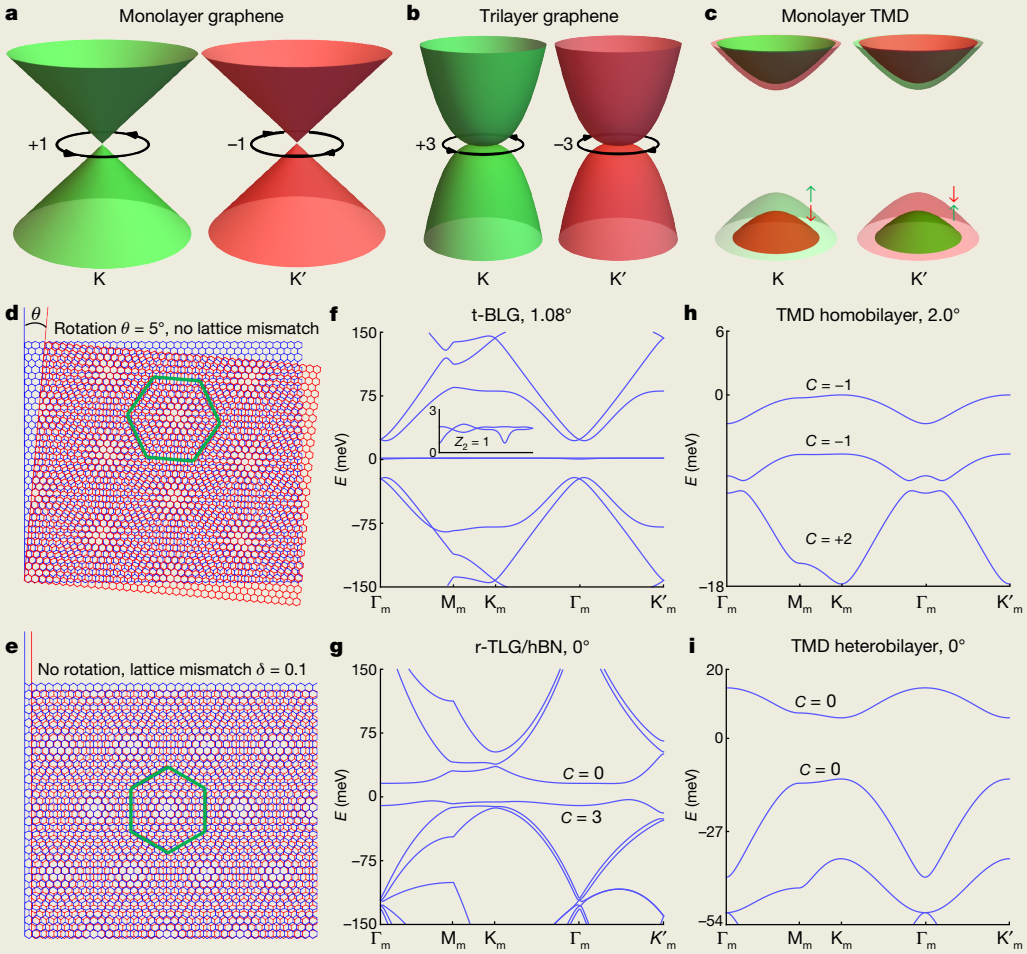

Panel **f** shows the t-BLG minibands for θ=1.08°. The Dirac minibands near zero energy (inset of panel **f**) are separated from high-energy minibands by two superlattice gaps. The Dirac velocity decreases to zero at the first magic angle of about 1.05° (ref. [62]). The superlattice gaps close below about 1°, where a series of secondary magic angles is predicted[62]. The band flatness at magic angles has deep connections to quantum Hall physics and index theorems[128], as the Dirac fermions propagate in an SU(2) non-Abelian gauge potential[129] from spatially modulated interlayer hopping. The first magic angle is unchanged or forms the basis of a hierarchy of magic angles for more complex graphene moiré systems[130,131]. Markedly, time-reversal (T) and two-fold rotational (C_{2z}) symmetries protect the two miniband Dirac points of the same winding number originating from the same principal valley but two different layers. The $C_{2z}T$ symmetry also protects unusual Z_2 band topology of the two Dirac minibands that has been evidenced in non-local transport[83–86]. The $C_{2z}T$ symmetry cannot be broken by a perpendicular displacement field D.

r-TLG is strongly interacting even without moiré engineering because of its much less dispersive bands and enjoys an interaction-driven or D-field-induced bandgap at the CNP[107,132]. In r-TLG/hBN, narrow bandwidths of about 10 meV are achievable for twist angles of θ<0.6° with interlayer potential differences of about 50 meV (ref. [127]). Panel **g** shows the minibands for θ=0°, with a gap at the CNP and valley Chern numbers of 0 and 3 for the two low-energy minibands. The D field can tune the gap size near Γ_m and thus control the bandwidth. For a TMD homobilayer, the topmost miniband can be

mapped to the Kane–Mele model, whereas other minibands can also enjoy non-trivial valley/spin Chern numbers that are sensitive to the twist angle[11]. Panel **h** shows the minibands of a 2H-$MoTe_2$ homobilayer for θ=2°. The first two minibands have a global gap smaller than 5 meV, and the Kane–Mele phase is robust up to a twist angle of about 3.1°. TMD heterobilayers, or homobilayers with large D fields, can be mapped to a single-band extended Hubbard model on a triangular lattice[14]. Panel **i** shows the minibands of a WSe_2/WS_2 heterobilayer for θ=0°. The highest miniband is localized around the triangular lattice of moiré potential maxima. While these two TMD moiré systems are derived from K-valley holes, TMD homobilayers of Γ-valley holes can create models on honeycomb and kagome lattices[119,133].

the crystal axis directions by non-invasive optical methods, such as angle-resolved second-harmonic generation (SHG), which is applicable to non-centrosymmetric materials[15,16]. Unlike graphene moiré systems, TMD bilayers with near 0° and 60° twist angles constitute distinct superlattices, which can be unambiguously distinguished via SHG; thus, another SHG imaging is needed to determine θ of the completed stack.

The disorder level of the TMD moiré materials is substantially influenced by the bulk crystal source; samples built on flux-grown crystals[39] are less disordered compared with those grown by chemical vapour

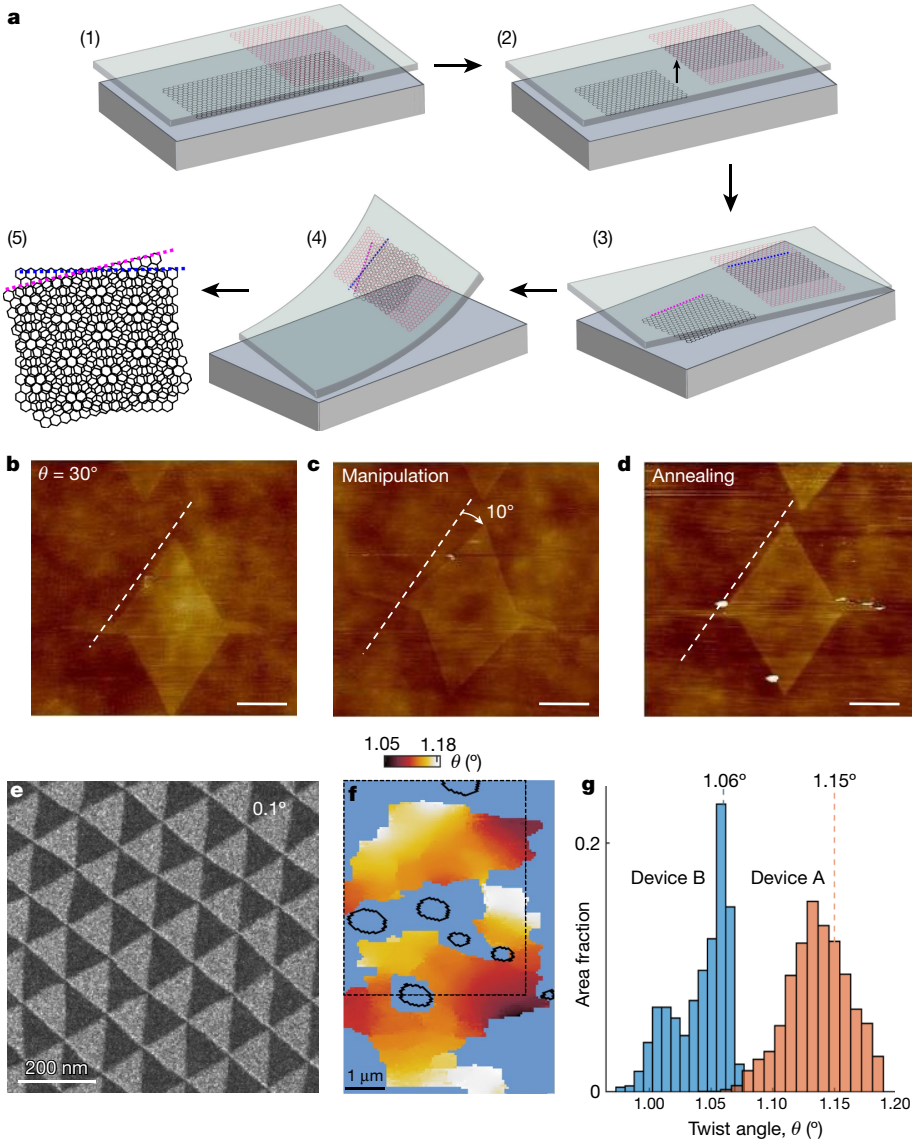

Fig. 2 | Fabrication of twisted bilayer graphene and various disorders in moiré systems. a, Schematics of the often-employed 'tear-and-stack' technique. (1). A polymer stamp with an hBN flake (red) approaches a large graphene flake (black) on a silicon (Si)/silicon dioxide (SiO_2) substrate. (2) The right half of the graphene flake is picked up by the hBN flake by van der Waals interactions, and the polymer stamp is lifted, hence tearing the graphene flake into two. (3) The graphene/hBN stack is moved over the part of the graphene flake left on the substrate, rotated by a small angle and lowered into contact. (4) The twisted bilayer/hBN stack is picked up from the polymer stack, then released onto a new substrate (not shown). (5) Schematic of twisted bilayer graphene lattices. The red and blue lines outline the lattice edges. **b**–**d**, AFM images of as-prepared 30°-twisted graphene/hBN (**b**), after manipulation of 10° rotation (**c**) and after 1 h of annealing at 400 °C (**d**). Scale bars, 400 nm. **e**, TEM dark-field image of t-BLG with θ = 0.1°. The alternating contrast of the AB/BA domains is associated with the antisymmetric shift of lattice period in the AB and BA domains. **f**, **g**, Two-dimensional map of the twist angle θ measured by scanning SQUID microscopy (**f**) and histogram of local θ in two different devices (**g**). The dashed lines mark the global θ derived from transport measurements. Panels reproduced with permission from: **b**–**d**, ref. [38], APS; **e**, ref. [59], Springer Nature Ltd; **f**, **g**, ref. [71], Springer Nature Ltd.

transport. Another challenge in TMD moiré materials is Schottky barrier formation, which often leads to poor contacts. Good contacts have been achieved for n-type molybdenum diselenide ($MoSe_2$; ref. [40]) or p-type WSe_2 (ref. [41]) by using platinum electrodes, and graphene electrodes are suitable for n-type molybdenum disulfide (MoS_2; ref. [42]) conduction. Also, increasing the moiré density by increasing the twist angle or the lattice mismatch is crucial, as the contact resistance is in general substantially reduced at high doping densities. So far, good p-type contacts for transport studies have been reported for homobilayer WSe_2 with large twist angles[13,43] and $MoTe_2/WSe_2$ with large lattice mismatch[44,45]. In addition, the use of local gates to induce high-doping-density regions that bridge the metal electrodes to the TMD channel is equally important to reduce the contact resistance.

For r-TLG/hBN heterobilayers, the crucial ABC domains are identified by scanning near-field infrared microscopy or Raman spectroscopy[46,47], and isolated from adjacent ABA domains by AFM cutting. The isolated r-TLG is then aligned to exfoliated hBN sheets to form the moiré superlattice. Notably, complete isolation of the ABC domains from the ABA domains is critical, otherwise an ABC domain is likely to structure transition into an ABA domain that has a lower energy. This has been a major issue in the reproducibility of strongly correlated physics in this system, despite much effort.

Relaxation, reconstruction and macroscopic rotation of lattices

One challenge in the fabrication of small θ moiré systems is that such atomic configurations are not the thermodynamic ground state, but only metastable. In the presence of superlubricity[48–51]—that is, vanishing interlayer friction between two misaligned atomic layers—the van der Waals forces will drive the system into the most stable ground state, for example, Bernal stacking for bilayer graphene. The phenomena of superlubricity and macroscopic rotation have been observed experimentally. For instance, upon annealing at 200–400 °C for a few hours, graphene is thermally induced to rotate on hBN towards lattice alignment when the twist angle is less than 12° (refs. [38,52,53]; Fig. 2b–d). Even at temperatures as low as 5 K, graphene nanoflakes are found to move and rotate rather freely on graphene surfaces[54]. As fabrication of 2D moiré systems involves elevated temperatures, for example, lithography resists are typically cured at 180 °C, these results suggest that the twist angle achieved in devices will be smaller than the target angle during fabrication, which is consistent with anecdotal reports.

Another metastability phenomenon is lattice relaxation and reconstruction, particularly for very small θ, as the heterostructure tends to maximize areas of AB stacking, which is energetically favoured, at the expense of AA stacking. For instance, a commensurate–incommensurate transition is observed when graphene and hBN lattices are almost aligned ($\theta \lesssim 1°$)[55]. In the commensurate phase, hexagonal lattice-matched domains are separated by domain walls where the strains in the stretched graphene lattice are accumulated. In the incommensurate phase, by contrast, the lattices remain essentially unperturbed. A similar commensurate phase is observed in minimally twisted bilayer graphene ($\theta \lesssim 0.5°$): the lattice reconstructs to form a triangular network of alternating domains of AB and BA stacking[56–59] (Fig. 2e). Recently, using Bragg interferometry based on scanning transmission electron microscopy[60], maps of atomic displacement and strain fields in t-BLG have revealed local rotational reconstruction, where rotations involving the AB and AA regions become dominant at $\theta \lesssim 0.5°$ and $\theta \gtrsim 0.5°$, respectively, consistent with the commensurate–incommensurate transitions[56–59]. At larger angles, although the commensurate phase is absent, three-dimensional buckling reconstruction together with periodic in-plane strain redistribution are observed in WSe_2/WS_2 heterobilayers[61]. These results suggest that a number of phenomena predicted for tiny-θ moiré systems, such as a series of smaller magic angles[62], the formation of pseudo-Landau levels and an emergent Kagome lattice[63], might only be achieved in realistic systems by inventing techniques to stabilize the lattices in the metastable state without reconstruction.

Angular and strain disorders

In realistic samples, inhomogeneities in the twist angle or lattice mismatch are ubiquitous. They constitute a type of disorder not found in conventional materials, with considerable effects on the properties of moiré systems. Notably, strain in a moiré superlattice is much amplified, by about $1/\delta$ in a heterobilayer or about $1/\theta$ in homobilayers, compared with the relative strain between the constituent materials.

For homobilayers, the moiré band structure (Box 1) is highly sensitive to θ and therefore twist angle disorder[2,11]. Angular disorder introduces variations in the filling factor ν of the moiré superlattices, which scales with θ^2 at constant charge density and determines the electronic phase of the system (see 'Reproducibility issues in electronic phases and properties of moiré materials'). This is especially true in t-BLG, in which flat bands are realized at only specific magic angles. Correlated electronic states, which are highly sensitive to the single-particle band structure, can be easily destabilized by angle disorder. In contrast, the moiré band structure in heterobilayers is largely determined by the lattice mismatch between the two layers[15,16], thus heterobilayers are relatively insensitive to twist angle disorder and tend to give more robust correlated electronic states.

Both heterobilayers and homobilayers are affected by heterostrains, that is, strains that differ in magnitude or direction in the two atomic layers. Such strains are presumably introduced inadvertently during the fabrication process, for example, through the 'tearing', pick-up or releasing steps, and upon metal deposition[64].

In transport measurements, angular disorder manifests as variations in the measured n_0 values (the charge density corresponding to one electron per unit cell) across different regions of a device. Recently, they have been visualized more directly by using Raman spectroscopy[65], scanning tunnelling microscopy (STM)[66–70], transmission electron microscopy (TEM)[56–59], scanning SQUID (superconducting quantum interference device) microscopy[71], scanning single electron transistor microscopy (s-SET)[72] and piezoelectric force microscopy[73]. These measurements reveal typical angular disorder of about ±0.1° and heterostrain of about 0.1–0.7% in micrometre-sized samples of t-BLG (Fig. 2f, g). Their precise impact on the electronic properties is not known (one recent theoretical calculation shows that their effect may be relatively modest[74]); nevertheless, they are widely believed to constitute the bottleneck of achieving reproducibly high-quality samples. For the next generation of devices, controlling and minimizing strain and angular disorder will be an important objective for further improvement in device quality and reproducibility.

Routes to optimizing device reproducibility

Looking afield, fulfilling the promise of moirétronics imperatively depends on the development of well-controlled and reproducible techniques yielding high-quality, uniform devices with minimal impurities, angular disorder, strain disorder and random lattice reconstruction. Although the authors do not have a crystal ball, some likely directions of improvement may come from the development of new polymers for the transfer process (ideally, the polymer should flow nicely when heated and have the right viscosity, adhesivity and rigidity, while leaving little residue), performing the transfer process in vacuum to eliminate bubble formation[75], and developing tools that enable quick, large-area and high-resolution characterization of θ and δ for quick feedback during fabrication. Efforts to automate the process, such as those already implemented to fabricate van der Waals heterostructures[76], will greatly increase the throughput and improve uniformity, and will certainly be a prerequisite if the field is to find any practical application.

For moiré heterobilayers, the angle-aligned structure is likely to be the stable/metastable configuration. Appropriate annealing of the fabricated devices, which typically have a small rotation angle from the perfect angle-aligned structure, can potentially relax the structure to the stable/metastable configuration and yield more homogeneous

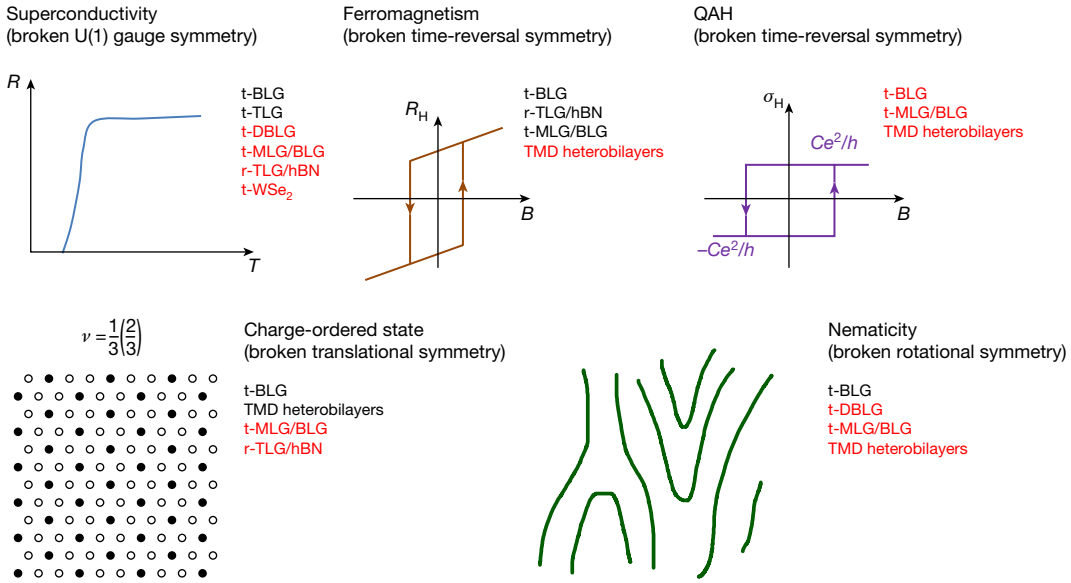

Fig. 3 | Schematics of various electronic phases and the systems in which they are observed. The systems in red indicate that the phenomena have been reported by only a single group at the time of writing. t-TLG, twisted trilayer graphene; t-DBLG, twisted double bilayer graphene; t-MLG/BLG, twisted monolayer/bilayer graphene; R, longitudinal resistance; T, temperature; R_H, Hall resistance; σ_H, Hall conductivity.

samples. Angle-aligned TMD heterobilayers can also be grown by chemical vapour deposition methods[77]. Homogeneous and angle-aligned materials can potentially be synthesized at large scales.

Moiré properties and reproducibility issues

The fascinating electronic phases of 2D moiré systems are complex and rapidly evolving as the field progresses. An important parameter in all moiré systems is the so-called filling factor, $\nu = n/n_0$, which refers to the extent to which the electron or hole bands are filled, and n_0 is the charge density corresponding to one electron per moiré unit cell. For graphene and TMD-based systems, it takes four and two charges per cell to fill each miniband, respectively. A variety of phases, such as superconductivity, correlated insulator, Chern insulator and emergent electron crystals have been observed (summarized in Fig. 3 for t-BLG, r-TLG/hBN and TMD systems)[78–80]. The nature, mechanism and exact phenomenology of the phases below full band filling are under intense experimental and theoretical debate, which is discussed below.

Superconductivity

The discovery of superconductivity in t-BLG is surprising, not only because it comes from non-superconducting 'parents'—pure carbon—but also because it occurs at very low charge density, about 1×10^{12} cm^{-2}, corresponding to an unusually high ratio of T_c/T_F (where T_c and T_F are the critical temperature and the Fermi temperature, respectively). Theoretically, although ultraflat bands are detrimental to the superfluid weight that determines a 2D superconductor's T_c (refs. [81,82]), the non-trivial flat band topology[83–86] substantially contributes to the superfluid weight[87–89] and yields an unusually high T_c/T_F in these moiré systems[2,90]. In t-BLG, superconductivity is found to be enhanced by pressure[91] and in the vicinity of insulating states at quarter fillings of the moiré band[92,93]. Recently, robust superconductivity has also been reported in twisted triple layers of graphene[21,22]. More ambiguous features resembling superconductivity have also been reported in platforms such as r-TLG/hBN[20], twisted double bilayer graphene[3], monolayer on bilayer graphene[9] and twisted bilayer WSe_2 (refs. [13,94]). However, in a recent report, superconductivity was not reproduced in high-quality r-TLG/hBN devices fabricated using the same protocol[36].

Superconductivity in magic-angle t-BLG away from integer filling is a robust and reproducible phenomenon. Figure 3a summarizes the observed superconducting domes in t-BLG so far. In early reports, on application of an out-of-plane magnetic field B, modulation of the critical current resembled that of the Fraunhofer pattern in a Josephson junction, that is, a weak link flanked by superconducting banks. Note that here the devices were not explicitly fabricated as a Josephson junction, and the Fraunhofer-like oscillations probably arise from percolating superconducting patchworks in an inhomogeneous device with, for example, angular and strain disorders. Recently, Josephson junctions that are created by applying different gate voltages to different regions of a single piece of t-BLG have been demonstrated[95,96]. These experimental results thus establish the macroscopic coherence of a condensate that is regarded as one of the key signatures of superconductivity.

By contrast, superconductivity in other moiré systems is less established and tends to be controversial. One issue is that theevidence for superconductivity is often taken to be the precipitous decrease in resistance and/or nonlinear current–voltagecharacteristics. However, such evidence is not definitive, as the reported superconducting state typically has low, but notnecessarily zero, resistance, and Joule heating may also give rise to nonlinear current–voltage curves. More importantly, asuperconductor is much more than a perfect conductor—it should also exhibit a well-defined superconducting gap, the formationof a condensate with macroscopic coherence and Meissner effect (expelling of magnetic flux below a critical field H ; foratomically thin 2D materials in the superconducting phase, they should exhibit diamagnetism that partially screens the magneticfield). Thus far, experimental demonstration of these hallmark traits has been lacking. In fact, one recent study on twisted doublebilayer graphene attributed the low-resistance state to the onset of a correlated state, not superconductivity [5]. Furtherexperimental investigation, such as persistent current measurements and demonstrating vortices hosting the superconducting fluxquantum, is necessary to provide definitive confirmation of superconductivity in non-t-BLG moiré systems. Mapping andcorrelating the twist angle with superconductivity and associated parameters (or the lack thereof) using tools such as STM andscanning SQUID microscopy that operate below 1 K will provide insight on the nature and mechanism of this remarkable phase.

Correlated insulating states

In moiré materials, insulating states are often observed at commensurate fractional fillings of the moiré minibands. These insulating states are not trivial band insulators, as energy gaps are not expected in single-particle theories. Rather, they arise from the strong Coulomb interactions and their interplay with symmetry and/or band topology in the flat minibands, and are therefore called correlated insulators. This 'catch all' phrase includes insulating phases that are topological and non-topological, magnetic and non-magnetic, ordered and disordered.

Magic-angle t-BLG. At low temperature, prominent resistance peaks are routinely observed in non-hBN-aligned magic-angle t-BLG devices at all integer filling factors ($-4 < \nu < 4$)[1,2,90,92,97]. Some of them are robust and even observed in a device with a relatively small twist angle of 0.93° (ref. [98]). Such correlated insulating states have also been observed at certain integer band fillings in twisted double bilayer graphene[3–7], monolayer–bilayer graphene[8–10] and triple layers of graphene[21,22]. Consistently, magneto-transport[93,99,100], high-resolution STM[70,101] and s-SET[72] measurements all reveal a cascade of phase transitions at all the integer fillings from −3 to 3, corresponding to flat minibands crossing the Fermi energy and resetting the massive Dirac-like character. The cascade of transitions characterizes the correlated high-temperature parent phases from which various insulating and superconducting ground states emerge at reduced temperatures.

Under magnetic fields, experiments[93,99,100,102] have further revealed a pronounced sequence of perfectly quantized correlated Chern insulators following the correspondence of (C, ν) of (±2, 0), (±4, 0), (±3, ±1), (±2, ±2) and (±1, ±3), where C is the first Chern number. This can be explained by a repeated occupancy of one miniband of $C = -1$ away from the charge neutrality point (CNP) at $\nu = 0$ but two zero-energy Landau levels of $C = 2$ near the CNP. The persistence of these Chern insulator states to $B = 0$ should give rise to quantum anomalous Hall (QAH) states with quantized Hall conductance Ce^2/h, where e is the electron charge and h is the Planck constant, although so far only imperfectly quantized Hall resistance of $C = \pm 1$ has been observed at $\nu = 1$ (ref. [93]). The corresponding QAH ground states maximize the Chern numbers and are favoured over other competing states in a magnetic field that couples to their quasiparticle orbital magnetization[107]. However, a recent s-SET measurement in one device has revealed a sequence of incompressible states with unexpected Chern numbers down to $B = 0$ (ref. [104]); this observation is incompatible with the established picture of sequential filling of the C = ±1 minibands.

hBN-aligned systems. In hBN-aligned t-BLG, QAH states with Chern number of ±1 and ferromagnetic hysteresis have been observed at $\nu = 3$ (refs. [103,105]). Scanning SQUID imaging of the sample reveals micrometre-sized magnetic domains[106], which may be related to the twist angle disorder. Consistently, the edge states with reversible chirality manifest in both transport and SQUID measurements. However, so far, quantized Hall resistance at $B = 0$ has been observed in only one device[103]. Presumably, angular and strain disorders destroy the perfect Hall quantization, thus reliable fabrication protocols of higher-quality devices are much needed.

In r-TLG/hBN, correlated insulating states have been observed at $\nu = -1$ and $\nu = -2$ in transport measurements[19–21] and at $\nu = \pm 1$ and $\nu = \pm 2$ in a capacitance measurement[36]. Consistently, in both types of measurement the only topologically non-trivial state is the $\nu = -1$ state with $C = 2$ at negative displacement fields. Interestingly, it appears that the moiré potential is not necessary for the emergence of these states[36].

Novel orbital magnetism accompanies all the aforementioned QAH states, like the predicted and observed ground states of BLG and its rhombohedral cousins[107–111]. In general, spontaneous gap opening at Dirac points produces and aligns quasiparticle orbital (instead of spin) magnetic moments with macroscopic coherence[107].

TMD. Correlated insulating states driven by flat-band physics have also been consistently reported in TMD moiré superlattices using optical, capacitance and transport measurements. Compared with graphene moiré superlattices, the orbital character of the moiré flat bands in TMD systems is simpler and lattice models can largely capture the flat-band physics. For non-topological flat bands, multiple experimental groups have reported the Mott and/or charge-transfer insulating states at half band filling in different TMD bilayers (for example, WSe_2/WS_2 and $MoTe_2/WSe_2$ heterobilayers, and WSe_2 and $MoSe_2$ homobilayers)[12,13,15,16]. The insulating state is driven by the strong on-site Coulomb interaction that favours electron localization. Tuning the local electronic interaction can further induce a continuous Mott transition, as demonstratedby two recent studies[43,44]. The magnetic ground state of the Mott insulator can be either a three-sublattice 120° Néel order or a quantum spin liquid[14]. In addition, topological flat bands have also been realized by intertwining two moiré bands in near-60°-aligned $MoTe_2/WSe_2$ heterobilayers[45]. A QAH insulator at half band filling and evidence of quantum spin Hall insulator at full band filling have been observed. The electric-field-tuned Mott-insulator-to-QAH-insulator quantum phase transition shows no charge gap closure. The nature of these topological states and the associated phase transitions require more in-depth investigations.

In addition to states at integer filling factors of the moiré superlattice, correlated insulating states have been observed by several groups at fractional fillings of the WSe_2/WS_2 and $MoSe_2/WS_2$ heterobilayers[15,17,112–114]. These states are charge-ordered states (or generalized Wigner crystal states) that spontaneously break the translation symmetry of the lattice to minimize the extended Coulomb repulsion between electrons. Searching for fractional states in other TMD moiré systems with topological flat bands and in graphene moiré systems with stronger interactions (for example, r-TLG/hBN[36]) are interesting future directions that could help realize fractional Chern insulators at zero magnetic field.

Nematicity

In a nematically ordered electron system, the electronic ground state spontaneously breaks rotational symmetry while retaining other symmetries such as translation and time-reversal symmetries[115]. In t-BLG, nematicity has been revealed by several STM studies, including charge stripe order near the CNP aligned along a two-fold axis that breaks the C_6 symmetry of t-BLG[69], rotational symmetry breaking in the measured local density of states[66,69,116], and a doping dependence that indicates a nematic phase most strongly developed near half filling[66]. These atomic-scale studies are partially corroborated by the only transport study reported so far[117]—the normal state of t-BLG devices shows anisotropic resistivity, whereas in the superconducting phase the critical current's dependence on the direction of an in-plane magnetic field shows a two-fold axis; this axis rotates as the doping density is varied by a gate voltage, suggesting intrinsic nematic correlations not driven by strain. Although other groups have yet to reproduce this result, nematic ordering above the superconducting T_c is consistent with the STM measurements.

A recent experiment has also reported the emergence of stripe crystals and electronic liquid crystals in WSe_2/WS_2 heterobilayers[118]. The result is consistent with theoretical predictions of nematic order in the correlated insulating states of TMD moiré systems[119]. What is at present unclear is the role played by strain in the observed nematicity; it is possible that strain is needed to stabilize the nematic phase or the stripe phase over macroscopic length scales and enable it to win over other competing ground states. In the future, direct correlation of devices' electronic and optical properties with high-resolution strain mapping by, for example, piezoelectric force microscopy[73], STM and TEM, will yield important insight into the nematic ordering found in moiré systems.

Outlook

The rapid progress of the field of moiré materials over the past three years has uncovered numerous phenomena, although many

questions and challenges remain under intense debate. Although the debates and challenges reflect the complexity and richness of 2D moiré systems, they also partly stem from the less-than-perfect reproducibility in the field. For instance, some electronic phases have been reported by only a single group and are yet to be reproduced by others; a number of published studies, including one by some of the authors, reported results obtained in a single device. As the field moves forward, these reproducibility issues should not be overlooked.

One particularly critical aspect of reproducibility is ensuring sample homogeneity and improving fabrication protocols, as outlined in 'Fabrication and experimental challenges'. Although the large-scale growth of angle-aligned heterobilayers, which are the thermodynamic ground states, is promising, large-scale production of homobilayers or heterobilayers with uniformly controlled angles and minimal lattice reconstruction remains challenging. To this end, establishing community-based portals for sharing 'know hows' will go a long way towards training students, optimizing existing protocols, developing new techniques and, ultimately, increasing reproducibility. The development of tools and techniques that enable correlation of lattice distortion and electronic properties (ideally from the same device) will yield important insight. Similarly, developing tools for direct visualization of the flat bands, energy gaps and orbital nature of minibands with improved energy, momentum, spatial and temporal resolutions will be crucial to further progress.

An interesting related development is the report of superconductivity and a fractional metal state in r-TLG[36,120], thus enabling the study of correlated phases in graphene without the fabrication issues related to twisted multilayers[107–111].

Looking ahead, many more opportunities are afoot, including homobilayers via applying heterostrains[121–123], twisted bilayers of non-hexagonal Bravais lattices[124], moiré magnets[125,126], moiré superconductors and so on. With the ever-increasing family of 2D materials and thousands of layer compounds that can thinned down to the atomic limit, and with improved reproducibility, the endless possibilities for correlated 'moirétronics' await theoretical, experimental, computational and technological exploration.

1. Cao, Y. et al. Correlated insulator behaviour at half-filling in magic-angle graphene superlattices. *Nature* **556**, 80–84 (2018).
2. Cao, Y. et al. Unconventional superconductivity in magic-angle graphene superlattices. *Nature* **556**, 43–50 (2018). **References [1,2] report the observation of a correlated insulating state and superconductivity in twisted bilayer graphene**.
3. Liu, X. et al. Tunable spin-polarized correlated states in twisted double bilayer graphene. *Nature* **583**, 221–225 (2020).
4. Burg, G. W. et al. Correlated insulating states in twisted double bilayer graphene. *Phys. Rev. Lett.* **123**, 197702 (2019).
5. He, M. et al. Symmetry breaking in twisted double bilayer graphene. *Nat. Phys.* **17**, 26–30 (2021).
6. Shen, C. et al. Correlated states in twisted double bilayer graphene. *Nat. Phys.* **16**, 520–525 (2020).
7. Cao, Y. et al. Tunable correlated states and spin-polarized phases in twisted bilayer–bilayer graphene. *Nature* **583**, 215–220 (2020).
8. Chen, S. et al. Electrically tunable correlated and topological states in twisted monolayer–bilayer graphene. *Nat. Phys.* **17**, 374–380 (2020).
9. Xu, S. et al. Tunable van Hove singularities and correlated states in twisted monolayer–bilayer graphene. *Nat. Phys.* **17**, 619–626 (2021).
10. Polshyn, H. et al. Electrical switching of magnetic order in an orbital Chern insulator. *Nature* **588**, 66–70 (2020).
11. Wu, F., Lovorn, T., Tutuc, E., Martin, I. & MacDonald, A. H. Topological insulators in twisted transition metal dichalcogenide homobilayers. *Phys. Rev. Lett.* **122**, 086402 (2019).
12. Shimazaki, Y. et al. Strongly correlated electrons and hybrid excitons in a moiré heterostructure. *Nature* **580**, 472–477 (2020).
13. Wang, L. et al. Correlated electronic phases in twisted bilayer transition metal dichalcogenides. *Nat. Mater.* **19**, 861–866 (2020).
14. Wu, F., Lovorn, T., Tutuc, E. & MacDonald, A. H. Hubbard model physics in transition metal dichalcogenide moiré bands. *Phys. Rev. Lett.* **121**, 026402 (2018). **This reference shows that the flat bands in moiré TMD structures can be described by generalized Hubbard models, and that a number of many-body ground states are possible**.
15. Regan, E. C. et al. Mott and generalized Wigner crystal states in WSe_2/WS_2 moiré superlattices. *Nature* **579**, 359–363 (2020).
16. Tang, Y. et al. Simulation of Hubbard model physics in WSe_2/WS_2 moiré superlattices. *Nature* **579**, 353–358 (2020). **References [15,16] report a Mott insulator in WSe_2/WS_2 bilayer superlattices at half filling, and generalized Wigner crystal and ferromagnetic states at fractional fillings**.
17. Xu, Y. et al. Correlated insulating states at fractional fillings of moiré superlattices. *Nature* **587**, 214–218 (2020).
18. Chen, G. et al. Evidence of a gate-tunable Mott insulator in a trilayer graphene moiré superlattice. *Nat. Phys.* **15**, 237–241 (2019). **This reference reports a gate-tunable insulator state in an r-TLG/hBN moiré superlattice at half filling**.
19. Chen, G. et al. Tunable correlated Chern insulator and ferromagnetism in a moiré superlattice. *Nature* **579**, 56–61 (2020).
20. Chen, G. et al. Signatures of tunable superconductivity in a trilayer graphene moiré superlattice. *Nature* **572**, 215–219 (2019).
21. Park, J. M., Cao, Y., Watanabe, K., Taniguchi, T. & Jarillo-Herrero, P. Tunable strongly coupled superconductivity in magic-angle twisted trilayer graphene. *Nature* **590**, 249–255 (2021).
22. Hao, Z. et al. Electric field–tunable superconductivity in alternating-twist magic-angle trilayer graphene. *Science* **371**, 1133–1138 (2021).
23. Hofstadter, D. R. Energy levels and wave functions of Bloch electrons in rational and irrational magnetic fields. *Phys. Rev. B* **14**, 2239–2249 (1976).
24. Yankowitz, M. et al. Emergence of superlattice Dirac points in graphene on hexagonal boron nitride. *Nat. Phys.* **8**, 382–386 (2012).
25. Ponomarenko, L. A. et al. Cloning of Dirac fermions in graphene superlattices. *Nature* **497**, 594–597 (2013).
26. Dean, C. R. et al. Hofstadter's butterfly and the fractal quantum Hall effect in moire superlattices. *Nature* **497**, 598–602 (2013).
27. Hunt, B. et al. Massive Dirac fermions and Hofstadter butterfly in a van der Waals heterostructure. *Science* **340**, 1427–1430 (2013).
28. Wang, P. et al. Topological winding number change and broken inversion symmetry in a Hofstadter's butterfly. *Nano Lett.* **15**, 6395–6399 (2015).
29. Kim, K. et al. Tunable moiré bands and strong correlations in small-twist-angle bilayer graphene. *Proc. Natl Acad. Sci. USA* **114**, 3364–3369 (2017).
30. Kim, K. et al. Van der Waals heterostructures with high accuracy rotational alignment. *Nano Lett.* **16**, 1989–1995 (2016).
31. Cao, Y. et al. Superlattice-induced insulating states and valley-protected orbits in twisted bilayer graphene. *Phys. Rev. Lett.* **117**, 116804 (2016).
32. Saito, Y., Ge, J., Watanabe, K., Taniguchi, T. & Young, A. F. Independent superconductors and correlated insulators in twisted bilayer graphene. *Nat. Phys.* **16**, 926–930 (2020).
33. Chen, X.-D. et al. High-precision twist-controlled bilayer and trilayer graphene. *Adv. Mater.* **28**, 2563–2570 (2016).
34. Pizzocchero, F. et al. The hot pick-up technique for batch assembly of van der Waals heterostructures. *Nat. Commun.* **7**, 11894 (2016).
35. Borodin, B. R., Benimetskiy, F. A. & Alekseev, P. A. Study of local anodic oxidation regimes in $MoSe_2$. *Nanotechnology* **32**, 155304 (2021).
36. Zhou, H. et al. Half and quarter metals in rhombohedral trilayer graphene. Preprint at https://arxiv.org/abs/2104.00653 (2021).
37. Rosenberger, M. R. et al. Nano-"squeegee" for the creation of clean 2D material interfaces. *ACS Appl. Mater. Interfaces* **10**, 10379–10387 (2018).
38. Wang, D. et al. Thermally induced graphene rotation on hexagonal boron nitride. *Phys. Rev. Lett.* **116**, 126101 (2016).
39. Gustafsson, M. V. et al. Ambipolar Landau levels and strong band-selective carrier interactions in monolayer WSe_2. *Nat. Mater.* **17**, 411–415 (2018).
40. Larentis, S. et al. Large effective mass and interaction-enhanced Zeeman splitting of K-valley electrons in $MoSe_2$. *Phys. Rev. B* **97**, 201407 (2018).
41. Fallahazad, B. et al. Shubnikov-de Haas oscillations of high-mobility holes in monolayer and bilayer WSe_2 Landau level degeneracy, effective mass, and negative compressibility. *Phys. Rev. Lett.* **116**, 086601 (2016).
42. Cui, X. et al. Multi-terminal transport measurements of MoS_2 using a van der Waals heterostructure device platform. *Nat. Nanotechnol.* **10**, 534–540 (2015).
43. Ghiotto, A. et al. Quantum criticality in twisted transition metal dichalcogenides. Preprint at https://arxiv.org/abs/2103.09796 (2021).
44. Li, T. et al. Continuous Mott transition in semiconductor moiré superlattices. Preprint at https://arxiv.org/abs/2103.09779 (2021).
45. Li, T. et al. Quantum anomalous Hall effect from intertwined moiré bands. Preprint at https://arxiv.org/abs/2107.01796 (2021).
46. Lui, C. H. et al. Imaging stacking order in few-layer graphene. *Nano Lett.* **11**, 164–169 (2011).
47. Cong, C. et al. Raman characterization of ABA- and ABC-stacked trilayer graphene. *ACS Nano* **5**, 8760–8768 (2012).
48. Dienwiebel, M. et al. Superlubricity of graphite. *Phys. Rev. Lett.* **92**, 126101 (2004).
49. Zheng, Q. et al. Self-retracting motion of graphite microflakes. *Phys. Rev. Lett.* **100**, 067205 (2008).
50. Liu, Z. et al. Observation of microscale superlubricity in graphite. *Phys. Rev. Lett.* **108**, 205503 (2012).
51. Yang, J. et al. Observation of high-speed microscale superlubricity in graphite. *Phys. Rev. Lett.* **110**, 255504 (2013).
52. Woods, C. R. et al. Macroscopic self-reorientation of interacting two-dimensional crystals. *Nat. Commun.* **7**, 10800 (2016).
53. Zhu, M. et al. Stacking transition in bilayer graphene caused by thermally activated rotation. *2D Mater.* **4**, 011013 (2016).
54. Feng, X., Kwon, S., Park, J. Y. & Salmeron, M. Superlubric sliding of graphene nanoflakes on graphene. *ACS Nano* **7**, 1718–1724 (2013).
55. Woods, C. R. et al. Commensurate–incommensurate transition in graphene on hexagonal boron nitride. *Nat. Phys.* **10**, 451–456 (2014). **This reference reports the commensurate–incommensurate transition in monolayer graphene at very small angles to the underlying hBN substrates**.

56. Brown, L. et al. Twinning and twisting of tri- and bilayer graphene. *Nano Lett.* **12**, 1609–1615 (2012).
57. Alden, J. S. et al. Strain solitons and topological defects in bilayer graphene. *Proc. Natl Acad. Sci. USA* **110**, 11256–11260 (2013).
58. Xu, S. G. et al. Giant oscillations in a triangular network of one-dimensional states in marginally twisted graphene. *Nat. Commun.* **10**, 4008 (2019).
59. Yoo, H. et al. Atomic and electronic reconstruction at the van der Waals interface in twisted bilayer graphene. *Nat. Mater.* **18**, 448–453 (2019).
60. Kazmierczak, N. P. et al. Strain fields in twisted bilayer graphene. *Nat. Mater.* **20**, 956–963 (2021).
This reference maps the strain fields and structural relaxation in t-BLG using Bragg interferometry.
61. Li, H. et al. Imaging moiré flat bands in three-dimensional reconstructed WSe_2/WS_2 superlattices. *Nat. Mater.* **20**, 945–950 (2021).
This reference demonstrates strong three-dimensional buckling reconstruction and large in-plane strain redistribution in WSe_2/WS_2 moiré heterostructures.
62. Bistritzer, R. & MacDonald, A. H. Moiré bands in twisted double-layer graphene. *Proc. Natl Acad. Sci. USA* **108**, 12233–12237 (2011).
This reference theoretically shows the presence of flat bands in t-BLG and predicts the magic angle of 1.05°.
63. Ramires, A. & Lado, J. L. Electrically tunable gauge fields in tiny-angle twisted bilayer graphene. *Phys. Rev. Lett.* **121**, 146801 (2018).
64. De Sanctis, A. et al. Strain-engineering of twist-angle in graphene/hBN superlattice devices. *Nano Lett.* **18**, 7919–7926 (2018).
65. Beechem, T. E., Ohta, T., Diaconescu, B. & Robinson, J. T. Rotational disorder in twisted bilayer graphene. *ACS Nano* **8**, 1655–1663 (2014).
66. Kerelsky, A. et al. Maximized electron interactions at the magic angle in twisted bilayer graphene. *Nature* **572**, 95–100 (2019).
67. Zhang, C. et al. Interlayer couplings, moiré patterns, and 2D electronic superlattices in MoS_2/WSe_2 hetero-bilayers. *Sci. Adv.* **3**, e1601459 (2017).
68. Xie, Y. et al. Spectroscopic signatures of many-body correlations in magic-angle twisted bilayer graphene. *Nature* **572**, 101–105 (2019).
69. Jiang, Y. et al. Charge order and broken rotational symmetry in magic-angle twisted bilayer graphene. *Nature* **573**, 91–95 (2019).
70. Choi, Y. et al. Electronic correlations in twisted bilayer graphene near the magic angle. *Nat. Phys.* **15**, 1174–1180 (2019).
71. Uri, A. et al. Mapping the twist-angle disorder and Landau levels in magic-angle graphene. *Nature* **581**, 47–52 (2020).
This reference maps the twist-angle disorder in t-BLG using scanning SQUID microscopy.
72. Zondiner, U. et al. Cascade of phase transitions and Dirac revivals in magic-angle graphene. *Nature* **582**, 203–208 (2020).
73. McGilly, L. J. et al. Visualization of moiré superlattices. *Nat. Nanotechnol.* **15**, 580–584 (2020).
74. Sainz-Cruz, H., Cea, T., Pantaleón, P. A. & Guinea, F. High transmission in twisted bilayer graphene with angle disorder. Preprint at https://arxiv.org/abs/2105.03383 (2021).
75. Lee, S. et al. Graphene transfer in vacuum yielding a high quality graphene. *Carbon* **93**, 286–294 (2015).
76. Masubuchi, S. et al. Autonomous robotic searching and assembly of two-dimensional crystals to build van der Waals superlattices. *Nat. Commun.* **9**, 1413 (2018).
77. Gong, Y. et al. Vertical and in-plane heterostructures from WS_2/MoS_2 monolayers. *Nat. Mater.* **13**, 1135–1142 (2014).
78. Liu, J. & Dai, X. Orbital magnetic states in moiré graphene systems. *Nat. Rev. Phys.* **3**, 367–382 (2021).
79. Andrei, E. Y. & MacDonald, A. H. Graphene bilayers with a twist. *Nat. Mater.* **19**, 1265–1275 (2020).
80. Balents, L., Dean, C. R., Efetov, D. K. & Young, A. F. Superconductivity and strong correlations in moiré flat bands. *Nat. Phys.* **16**, 725–733 (2020).
81. Liang, L. et al. Band geometry, Berry curvature, and superfluid weight. *Phys. Rev. B* **95**, 024515 (2017).
82. Peotta, S. & Törmä, P. Superfluidity in topologically nontrivial flat bands. *Nat. Commun.* **6**, 8944 (2015).
83. Ma, C. et al. Moiré band topology in twisted bilayer graphene. *Nano Lett.* **20**, 6076–6083 (2020).
84. Song, Z. et al. All magic angles in twisted bilayer graphene are topological. *Phys. Rev. Lett.* **123**, 036401 (2019).
85. Po, H. C., Zou, L., Senthil, T. & Vishwanath, A. Faithful tight-binding models and fragile topology of magic-angle bilayer graphene. *Phys. Rev. B* **99**, 195455 (2019).
86. Ahn, J., Park, S. & Yang, B.-J. Failure of Nielsen–Ninomiya theorem and fragile topology in two-dimensional systems with space-time inversion symmetry: application to twisted bilayer graphene at magic angle. *Phys. Rev. X* **9**, 021013 (2019).
87. Hu, X., Hyart, T., Pikulin, D. I. & Rossi, E. Geometric and conventional contribution to the superfluid weight in twisted bilayer graphene. *Phys. Rev. Lett.* **123**, 237002 (2019).
88. Julku, A., Peltonen, T. J., Liang, L., Heikkilä, T. T. & Törmä, P. Superfluid weight and Berezinskii–Kosterlitz–Thouless transition temperature of twisted bilayer graphene. *Phys. Rev. B* **101**, 060505 (2020).
89. Xie, F., Song, Z., Lian, B. & Bernevig, B. A. Topology-bounded superfluid weight in twisted bilayer graphene. *Phys. Rev. Lett.* **124**, 167002 (2020).
90. Tian, H. et al. Evidence for flat band Dirac superconductor originating from quantum geometry. Preprint at https://arxiv.org/abs/2112.13401 (2021).
91. Yankowitz, M. et al. Tuning superconductivity in twisted bilayer graphene. *Science* **363**, 1059–1064 (2019).
92. Lu, X. et al. Superconductors, orbital magnets and correlated states in magic-angle bilayer graphene. *Nature* **574**, 653–657 (2019).
This reference reports the observation of a correlated insulating state, orbital magnetism and superconductivity at every integer filling of t-BLG.
93. Stepanov, P. et al. Competing zero-field Chern insulators in superconducting twisted bilayer graphene. Preprint at https://arxiv.org/abs/2012.15126 (2020).
94. An, L. et al. Interaction effects and superconductivity signatures in twisted double-bilayer WSe_2. *Nanoscale Horiz.* **5**, 1309–1316 (2020).
95. Rodan-Legrain, D. et al. Highly tunable junctions and nonlocal Josephson effect in magic angle graphene tunneling devices. Preprint at https://arxiv.org/abs/2011.02500 (2020).
96. Vries, F. K. D. et al. Gate-defined Josephson junctions in magic-angle twisted bilayer graphene. Preprint at https://arxiv.org/abs/2011.00011 (2020).
97. Stepanov, P. et al. Untying the insulating and superconducting orders in magic-angle graphene. *Nature* **583**, 375–378 (2020).
98. Codecido, E. et al. Correlated insulating and superconducting states in twisted bilayer graphene below the magic angle. *Sci. Adv.* **5**, eaaw9770 (2019).
99. Wu, S., Zhang, Z., Watanabe, K., Taniguchi, T. & Andrei, E. Y. Chern insulators, van Hove singularities and topological flat bands in magic-angle twisted bilayer graphene. *Nat. Mater.* **20**, 488–494 (2021).
100. Saito, Y. et al. Hofstadter subband ferromagnetism and symmetry-broken Chern insulators in twisted bilayer graphene. *Nat. Phys.* **17**, 478–481 (2021).
101. Wong, D. et al. Cascade of electronic transitions in magic-angle twisted bilayer graphene. *Nature* **582**, 198–202 (2020).
102. Nuckolls, K. P. et al. Strongly correlated Chern insulators in magic-angle twisted bilayer graphene. *Nature* **588**, 610–615 (2020).
103. Serlin, M. et al. Intrinsic quantized anomalous Hall effect in a moiré heterostructure. *Science* **367**, 900–903 (2020).
This reference reports the observation of an intrinsic QAH state (that is, without magnetic dopants) in t-BLG aligned to hBN.
104. Pierce, A. T. et al. Unconventional sequence of correlated Chern insulators in magic-angle twisted bilayer graphene. Preprint at https://arxiv.org/abs/2101.04123 (2021).
105. Sharpe, A. L. et al. Emergent ferromagnetism near three-quarters filling in twisted bilayer graphene. *Science* **365**, 605–608 (2019).
106. Tschirhart, C. L. et al. Imaging orbital ferromagnetism in a moiré Chern insulator. Preprint at https://arxiv.org/abs/2006.08053 (2020).
107. Zhang, F., Jung, J., Fiete, G. A., Niu, Q. A. & MacDonald, A. H. Spontaneous quantum Hall states in chirally stacked few-layer graphene systems. *Phys. Rev. Lett.* **106**, 156801 (2011).
108. Velasco, J. et al. Transport spectroscopy of symmetry-broken insulating states in bilayer graphene. *Nat. Nanotechnol.* **7**, 156–160 (2012).
109. Shi, Y. et al. Electronic phase separation in multilayer rhombohedral graphite. *Nature* **584**, 210–214 (2020).
110. Lee, Y. et al. Gate tunable magnetism and giant magnetoresistance in ABC-stacked few-layer graphene. Preprint at https://arxiv.org/abs/1911.04450 (2019).
111. Geisenhof, F. R. et al. Quantum anomalous Hall octet driven by orbital magnetism in bilayer graphene. *Nature* **598**, 53–58 (2021).
112. Jin, C. et al. Stripe phases in WSe_2/WS_2 moiré superlattice. Preprint at https://arxiv.org/abs/2007.12068 (2020).
113. Huang, X. et al. Correlated insulating states at fractional fillings of the WS_2/WSe_2 moiré lattice. Preprint at https://arxiv.org/abs/2007.11155 (2020).
114. Li, T. et al. Charge-order-enhanced capacitance in semiconductor moiré superlattices. Preprint at https://arxiv.org/abs/2102.10823 (2021).
115. Fradkin, E., Kivelson, S. A., Lawler, M. J., Eisenstein, J. P. & Mackenzie, A. P. Nematic Fermi fluids in condensed matter physics. *Annu. Rev. Condens. Matter Phys.* **1**, 153–178 (2010).
116. Li, S.-Y. et al. Splitting of van Hove singularities in slightly twisted bilayer graphene. *Phys. Rev. B* **96**, 155416 (2017).
117. Cao, Y. et al. Nematicity and competing orders in superconducting magic-angle graphene. Preprint at https://arxiv.org/abs/2004.04148 (2020).
118. Jin, C. et al. Stripe phases in WSe_2/WS_2 moire superlattices. Preprint at https://arxiv.org/abs/2007.12068 (2020).
119. Xian, L. et al. Realization of nearly dispersionless bands with strong orbital anisotropy from destructive interference in twisted bilayer MoS_2. Preprint at https://arxiv.org/abs/2004.02964 (2020).
120. Zhou, H., Xie, T., Taniguchi, T., Watanabe, K. & Young, A. F. Superconductivity in rhombohedral trilayer graphene. Preprint at https://arxiv.org/abs/2106.07640 (2021).
121. Qiao, J.-B., Yin, L.-J. & He, L. Twisted graphene bilayer around the first magic angle engineered by heterostrain. *Phys. Rev. B* **98**, 235402 (2018).
122. Huder, L. et al. Electronic spectrum of twisted graphene layers under heterostrain. *Phys. Rev. Lett.* **120**, 156405 (2018).
123. Shi, H. et al. Large-area, periodic, and tunable intrinsic pseudo-magnetic fields in low-angle twisted bilayer graphene. *Nat. Commun.* **11**, 371 (2020).
124. Kariyado, T. & Vishwanath, A. Flat band in twisted bilayer Bravais lattices. *Phys. Rev. Res.* **1**, 033076 (2019).
125. Hejazi, K., Luo, Z.-X. & Balents, L. Noncollinear phases in moiré magnets. *Proc. Natl Acad. Sci. USA* **117**, 10721–10426 (2020).
126. Xu, Y. et al. Emergence of a noncollinear magnetic state in twisted bilayer CrI_3. Preprint at https://arxiv.org/abs/2103:09850 (2021).
127. Chittari, B. L., Chen, G., Zhang, Y., Wang, F. & Jung, J. Gate-tunable topological flat bands in trilayer graphene boron-nitride moiré superlattices. *Phys. Rev. Lett.* **122**, 016401 (2019).
128. Tarnopolsky, G., Kruchkov, A. J. & Vishwanath, A. Origin of magic angles in twisted bilayer graphene. *Phys. Rev. Lett.* **122**, 106405 (2019).
129. San-Jose, P., González, J. & Guinea, F. Non-Abelian gauge potentials in graphene bilayers. *Phys. Rev. Lett.* **108**, 216802 (2012).
130. Liu, J., Ma, Z., Gao, J. & Dai, X. Quantum valley Hall effect, orbital magnetism, and anomalous Hall effect in twisted multilayer graphene systems. *Phys. Rev. X* **9**, 031021 (2019).
131. Khalaf, E., Kruchkov, A. J., Tarnopolsky, G. & Vishwanath, A. Magic angle hierarchy in twisted graphene multilayers. *Phys. Rev. B* **100**, 085109 (2019).

132. Bao, W. et al. Stacking-dependent band gap and quantum transport in trilayer graphene. *Nat. Phys.* **7**, 948–952 (2011).
133. Angeli, M. & MacDonald, A. H. Γ valley transition metal dichalcogenide moiré bands. *Proc. Natl Acad. Sci. USA* **118**, e2021826118 (2021).

Acknowledgements C.N.L. acknowledges support from the Department of Energy under grant number DOE DE-SC0020187. M.W.B. acknowledges support from the National Science Foundation under grant numbers DMR 2004801 and DMR-2105028. F.Z. acknowledges support from the Army Research Office under grant number W911NF-18-1-0416 and the National Science Foundation under grant numbers DMR-1945351, DMR-2105139 and DMR-1921581. K.F.M. acknowledges support from the Air Force Office of Scientific Research under award number FA9550-20-1-0219.

Author contributions C.N.L., M.W.B., K.F.M. and F.Z. discussed and co-wrote the manuscript.

Competing interests The authors declare no competing interests.

Additional information
Correspondence and requests for materials should be addressed to Chun Ning Lau.
Peer review information *Nature* thanks Roman Gorbachev and the other, anonymous, reviewer(s) for their contribution to the peer review of this work.
Reprints and permissions information is available at http://www.nature.com/reprints.
Publisher's note Springer Nature remains neutral with regard to jurisdictional claims in published maps and institutional affiliations.